THE JOURNAL OF PHYSICAL CHEMISTRY LETTERS
A JOURNAL OF THE AMERICAN CHEMICAL SOCIETY

pubs.acs.org/JPCL Letter

Giant Bulk Photovoltaic Effect in Penta-$PdTe_2$ Induced by Layer Stacking

Changsheng Hou, Jiaqi Xin, Yiheng Shen,* Yaguang Guo,* and Qian Wang*

Cite This: *J. Phys. Chem. Lett.* 2025, 16, 7177−7186 Read Online

ACCESS | Metrics & More | Article Recommendations | Supporting Information

ABSTRACT: Stacking engineering has emerged as an effective strategy for tuning the physical properties of layered materials. Inspired by the recent experimental synthesis of penta-$PdTe_2$ sheets [Liu, L.; et al. *Nat. Mater.* **2024**, *23*, 1339], we demonstrate, based on systematic symmetry analysis and first-principles calculations, that bilayer penta-$PdTe_2$ exhibits a strong in-plane polarization; in particular, its ground state possesses a prominent spontaneous polarization ($P_s^y = 1.70 \times 10^{-10}$ C m^{-1}), leading to a giant shift current with a value as high as 125.49 μA V^{-2}, which is much larger than the corresponding values of bilayer penta-$PdSe_2$ (43.86 μA V^{-2}) and penta-PdS_2 (29.17 μA V^{-2}). The underlying mechanism is further elucidated through an analysis of the transition intensity and shift vector distributions in reciprocal space as well as the charge transfer of the *X* (X = Te, Se, or S) dimers in real space. Our findings highlight pentagonal materials as a promising platform for designing polar materials with strong bulk photovoltaic effect responses.

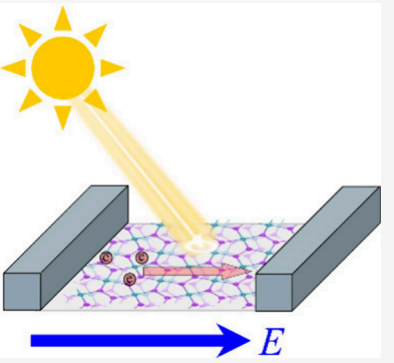

The photovoltaic effect, which enables the direct conversion of light into electricity, has attracted significant attention due to the growing demand for clean and renewable energy solutions. Among various photocurrent conversion mechanisms, the bulk photovoltaic effect (BPVE) is particularly promising, as it can occur in a single material without requiring doping.[1−3] Unlike p−n junctions, the photovoltage generated by BPVE is not constrained by the Shockley−Queisser limit, and BPVE can produce an open-circuit voltage exceeding the band gap, making it highly attractive for high-efficiency solar cells.[4] Early studies have shown that the photocurrent collection via BPVE with an efficiency larger than 10% can be achieved in the first-order photovoltaic effect in ferroelectric hybrid and oxide perovskites, which has motivated considerable research on ferroelectric photovoltaics.[5,6] From a physical perspective, BPVE is a second-order nonlinear optical response;[7] i.e., $j^a = \sigma^{abc}(\omega) E_b(\omega) E_c^*(\omega)$, where j^a represents the current density component in the *a* direction, $E_b(\omega)$ and $E_c(\omega)$ denote the component of the light electric field in the *b* and *c* directions, respectively, while σ (ω) is for the shift current conductivity tensor. The dominant factor for BPVE is the shift current, which arises from the difference in the wave function centers between the valence and conduction bands upon photoexcitation.[8,9] This fundamental requirement restricts BPVE to noncentrosymmetric materials.[3]

Polar materials are of particular interest for BPVE applications, as their intrinsic electric polarization can facilitate shift current generation under both polarized and nonpolarized light illumination,[10] thereby enhancing the BPVE response. Consequently, numerous two-dimensional (2D) polar materials have been experimentally synthesized or theoretically predicted as promising BPVE candidates, including single-layer group IV monochalcogenides,[11] 2D hybrid perovskites $[CH_3(CH_2)_3NH_3]_2(CH_3NH_3)Pb_2Br_7$,[12] α-In_2Se_3,[13] and $CuInP_2S_6$.[14] However, most 2D single-layer materials are centrosymmetric and thus lack BPVE properties. This limitation can be overcome through specific layer stacking configurations,[15] significantly expanding the pool of 2D materials suitable for BPVE applications. Recent theoretical advancements have established a generalized group theory framework for bilayer stacking ferroelectricity (BSF),[16] providing a systematic approach for predicting and designing polar materials with enhanced BPVE performance.

Beyond stacking-induced symmetry breaking, incorporating low-symmetry structural motifs has emerged as a key strategy in the rational design of polar materials. Since the theoretical proposal of penta-graphene (PG) in 2015,[17] substantial efforts have been dedicated to designing and synthesizing over 210 new 2D pentagonal materials.[18,19] Compared with conventional hexagonal 2D materials, pentagonal materials exhibit more complex atomic coordination environments that facilitate the formation of polar bonds. The reduced symmetry of pentagonal motifs, in contrast to hexagonal ones, enables the emergence of spontaneous polarization. The unique geometry of these pentagonal materials naturally facilitates electric

Received: May 18, 2025
Revised: June 27, 2025
Accepted: July 1, 2025

https://doi.org/10.1021/acs.jpclett.5c01522
J. Phys. Chem. Lett. 2025, 16, 7177−7186

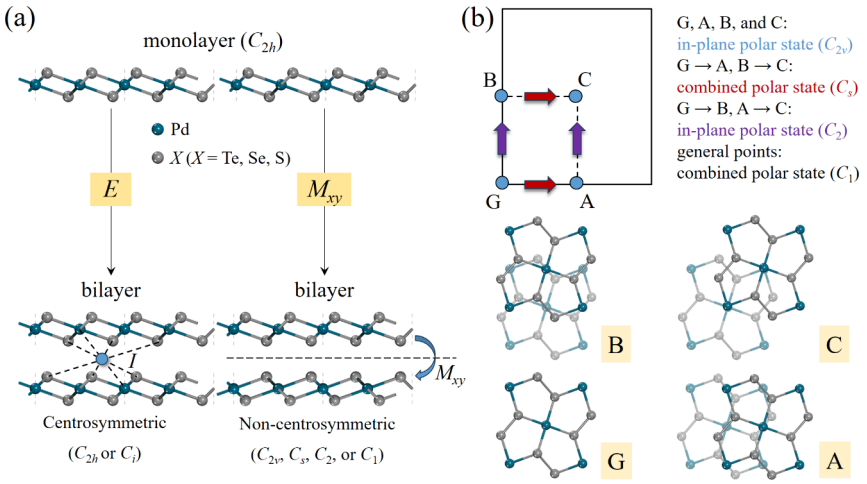

Figure 1. (a) Two simply stacked bilayer penta-PdX_2 (X = Te, Se, S) structures. (b) Symmetry analysis of the bilayer penta-PdX_2 (X = Te, Se, S) sheet along with the mirror plane M_{xy}, with the top view of the stacking configurations for translation points G (0, 0), A ($\frac{1}{2}$ $\boldsymbol{a}$, 0), B (0, $\frac{1}{2}$ $\boldsymbol{b}$), and C ($\frac{1}{2}$ $\boldsymbol{a}$, $\frac{1}{2}$ $\boldsymbol{b}$).

polarization, positioning them as highly promising candidates for BPVE applications.[20−23] Furthermore, sliding ferroelectricity was recently proposed in the penta-$PdSe_2$/penta-$PtSe_2$ van der Waals heterostructure[24] and trilayer penta-NiN_2,[25] further expanding the scope of pentagonal materials in BPVE application.

Motivated by the recent experimental synthesis of penta-$PdTe_2$,[26] we systematically explored the evolution of electric polarization across all possible stacking configurations of bilayer penta-$PdTe_2$ through symmetry analysis. Additionally, we confirmed that the ground state of bilayer penta-$PdTe_2$ exhibits in-plane electric polarization with strong BPVE responses through density functional theory (DFT) based first-principles calculations.

We perform first-principles calculations using the Vienna *ab initio* simulations package based on density functional theory (DFT).[27] The exchange−correlation interaction is treated with the generalized gradient approximation within the Perdew−Burke−Ernzerhof form.[28] The projector augmented wave method is used for describing the interaction between valence electrons and ion cores.[29] The valence electrons are expanded by a plane-wave basis set with its kinetic energy cutoff of 450 eV. We adopt the dispersion correction for the total energy (DFT-D3 scheme)[30] to semiempirically include the vdW interactions. The vacuum space of 25 Å is added along the nonperiodic direction of the primitive cell to avoid interactions between neighboring images. The first Brillouin zone is sampled by using a Monkhorst−Pack *k*-point mesh with a grid of 9 × 9 × 1.[31] All the structures are fully optimized with a convergence threshold of 1 × 10^{-4} eV $Å^{-1}$ for force and 1 × 10^{-6} eV for energy. The Heyd−Scuseria−Ernzerhof (HSE06) hybrid functional[32] is used for calculating the electronic band structures. The finite displacement method[33] implemented in the Phonopy code[34] is used for calculating the phonon spectra of structures using their 4 × 4 × 1 supercells. *Ab initio* molecular dynamics (AIMD) simulations for these systems are performed using the canonical ensemble with a Nosé−Hoover thermostat.[35] To avoid the uncertainty of stability caused by the constraints of periodic boundary conditions, 3 × 3 × 1 supercells were used in the AIMD simulations. The electric polarization is calculated with the Berry phase method.[36] The generation pathway of electric polarization is computed by using the climbing-image nudged elastic band method.[37] Bader charge analysis is used to grant insights into the electronegativity and quantify the charge distribution of the bilayer stacking structures.[38,39]

Our calculations of the nonlinear photocurrent responses, including both shift current and injection current, are derived from the nonlinear response theory within the independent-particle approximation.[40] The numerical approach uses maximal Wannier functions for interpolation, which ensures gauge invariance and facilitates efficient integration over the Brillouin zone.[41]

To evaluate the shift current generation, we fit the DFT results in the WANNIER90 code package.[42,43] The shift current photoconductance under linearly polarized light is evaluated by[7,41]

$$\sigma^{abb}(\omega) = -\frac{i\pi e^3}{\hbar^2}\int \frac{\mathrm{d}k}{8\pi^3}\sum_{n,m} f_{nm} r^b_{mn} r^b_{nm;a} \times \delta(\omega_{mn} - \omega)\cdot \left(\frac{d_z}{d_t}\right) \quad (1)$$

where *a* and *b* are Cartesian indices, representing the direction of photocurrent and polarization direction of the incident light, respectively. For the 2D system, *a*, *b* = *x* or *y*. *k* is the crystal momentum, *n* and *m* are the band indexes, f_{nm} is the difference between their Fermi−Dirac occupation numbers, and $\hbar\omega_{mn}$ is the band energy difference. The terms r^b_{nm} and $r^b_{nm;a}$ are both quantities associated with the Berry connection of the Bloch wave functions, referring to the dipole matrix element and its generalized derivatives, respectively. The coefficient d_z/d_t is used for a quantitative comparison between 2D and bulk systems, where d_z is the lattice constant perpendicular to the periodic plane and d_t is the thickness of the 2D structure.

In nonmagnetic systems, injection current is mainly induced by circularly polarized light (CPL); the injection current under CPL irradiation is evaluated by[44]

https://doi.org/10.1021/acs.jpclett.5c01522
J. Phys. Chem. Lett. 2025, 16, 7177−7186

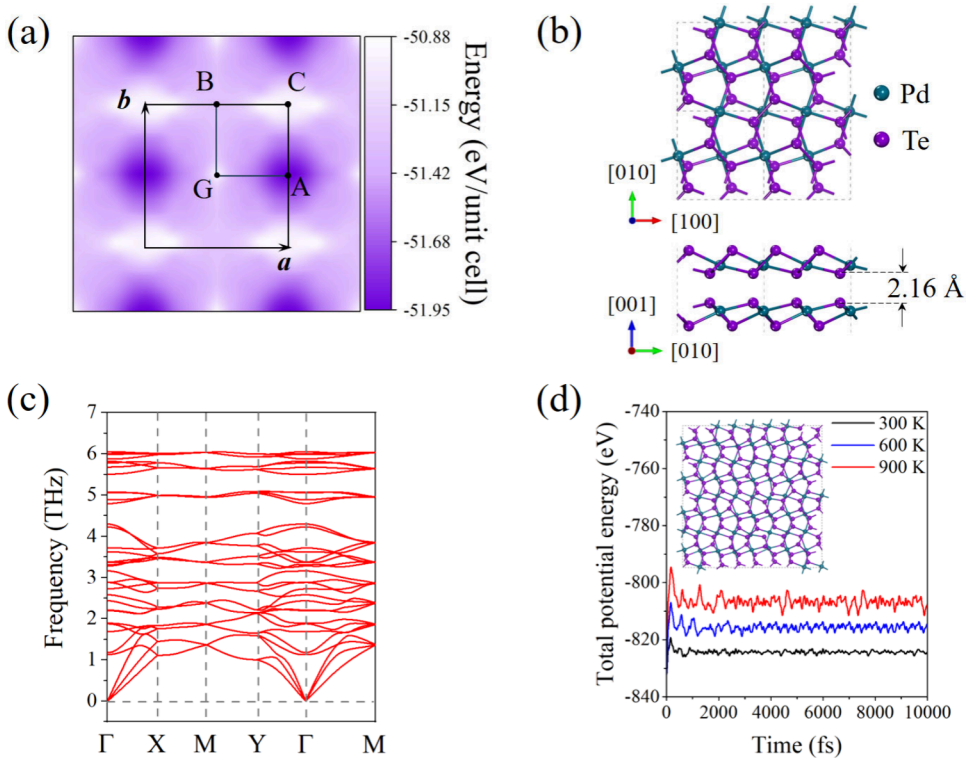

Figure 2. Potential energy surface associated with the interlayer sliding of the bilayer penta-$PdTe_2$. (b) Top and side views, (c) phonon spectrum, and (d) evolution of the total potential energy with simulation time during the AIMD simulations at 300, 600, and 900 K for bilayer penta-$PdTe_2$. The inset is the top view of the bilayer penta-$PdTe_2$ supercell at the end of the simulation at 900 K.

$$\eta^{abc}(\omega) = \frac{\mathrm{d}}{\mathrm{d}t}\sigma^{abc}(\omega) = -\frac{\pi e^3}{2\hbar^2}\int \frac{\mathrm{d}^2k}{(2\pi)^2} \times \mathrm{Im}\sum_{n,m} f_{nm}\Delta^a_{nm}[r^b_{mn}, r^c_{nm}]\delta(\omega_{mn} - \omega)\cdot\left(\frac{d_z}{d_t}\right) \quad (2)$$

where $\Delta^a_{nm} = \nu^a_{nn} - \nu^a_{mm}$ is the group velocity difference between the m^{th} and n^{th} bands.

Recently, monolayer penta-$PdTe_2$ with a Cairo tessellation structure was successfully synthesized through symmetry-driven epitaxy growth.[26] Notably, this monolayer shares the same C_{2h} symmetry as the previously synthesized penta-$PdSe_2$[45] and penta-PdS_2[46] monolayers, collectively classified as penta-PdX_2 (X = Te, Se, S). According to Neumann's principle,[47] the symmetry elements governing any physical property of a crystal must include all the symmetry elements of the crystal's point group. Theoretical analysis reveals that bilayer structures of penta-PdX_2 follow identical symmetry creation and annihilation rules when subjected to equivalent sliding vectors. Although the monolayer penta-PdX_2 belongs to the $c2/m11$ centrosymmetric layer group (no. 18), its bilayer counterparts, depending on their stacking configurations, can exhibit three distinct polarization types: in-plane polarization, a combination of in-plane and out-of-plane polarization, or nonpolar state, based on the BSF theory.[16]

For a simply stacked bilayer (i.e., without any relative translation), there are two possible stacking configurations, as illustrated in Figure 1a. In the first configuration, the two layers are stacked with identity symmetry, while in the second configuration, they are related by mirror plane M_{xy}. It can be seen that any pure translation $\hat{O} = \{E|\tau_0\}$ (including $\{E|\tau_0\}G_{S0}$) cannot break the inversion symmetry of the centrosymmetric monolayer. Consequently, the bilayer penta-PdX_2 can only possess C_{2h} or C_i symmetry, suggesting that spontaneous polarization is impossible based on $\hat{O} = \{E|\tau_0\}$. Here, $\hat{O}$ represents the transformation operator, τ_0 is the in-plane translational part, and G_{S0} is the point group of the monolayer, while the mirror reflection M_{xy} enforces symmetry breakage in bilayers, enabling the bilayer penta-PdX_2 to adopt C_{2v}, C_s, C_2, or C_1 polar symmetry under the translation $\hat{O} = \{M_{xy}|\tau_0\}$, which may induce spontaneous polarization in the bilayer penta-PdX_2. Therefore, we focus on bilayer penta-PdX_2 with mirror plane M_{xy} symmetry for further investigation.

As illustrated in Figure 1b, four typical stacking configurations exhibit in-plane polarization under C_{2v} symmetry, represented by sliding vectors G (0, 0), A ($\frac{1}{2}$ ***a***, 0), B (0, $\frac{1}{2}$ ***b***), and C ($\frac{1}{2}$ ***a***, $\frac{1}{2}$ ***b***), where ***a*** and ***b*** are the lattice vectors. The G, A, B, and C stacked bilayers exhibit in-plane polarization under C_{2v} symmetry. Additionally, sliding vectors along the G → B and A → C paths correspond to stacked bilayers with in-plane polarization under the C_2 symmetry, those along the G → A and B → C paths exhibit combined polarization under C_s symmetry, and the bilayers with general sliding vectors exhibit combined polarization under the C_1 symmetry. The controlled synthesis and precise tuning of bilayer stacking configurations can be realized through several experimental approaches, including strain engineering combined with chemical vapor deposition (CVD) growth,[48] scanning tunneling microscope (STM) tip-assisted manipulation,[49] and electric-field-driven interlayer sliding.[50] Since bilayer penta-PdX_2 (X = Te, Se, S) exhibits polarized states that depend on stacking geometry,

https://doi.org/10.1021/acs.jpclett.5c01522
J. Phys. Chem. Lett. 2025, 16, 7177−7186

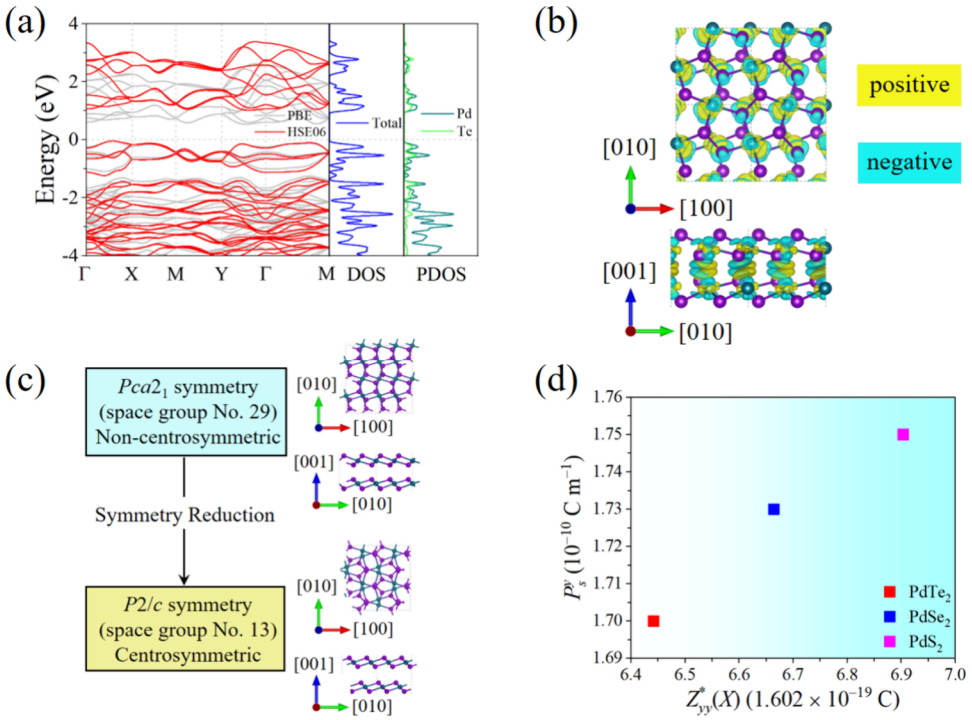

Figure 3. (a) Electronic band structure, DOS, and PDOS and (b) spatial distribution of the deformation charge density of the bilayer penta-$PdTe_2$ sheet (the isosurface value is ± 0.007 $Å^{-3}$. Yellow and blue regions represent charge gain and loss, respectively). (c) Searching for centrosymmetric paraelectric phases in bilayer penta-PdX_2 (X = Te, Se, S). (d) Relationship between the spontaneous polarization and Born effective charge $Z^*_{yy}(X)$ of bilayer penta-PdX_2 (X = Te, Se, S).

strategically modulating stacking configurations in these pentagonal layered materials offers a promising approach for designing efficient BPVE materials.

DFT calculations were performed to study the energetics and stability of the different stacking configurations. For the monolayer penta-PdX_2, the calculated results are presented in Figure S1 in the Supporting Information, which is in agreement with previous studies.[51] The configuration space of bilayer penta-PdX_2 is explored by keeping the bottom layer in the G stacking pattern fixed and sliding the top layer by $\boldsymbol{r} = (m\boldsymbol{a} + n\boldsymbol{b})/10$, where $m, n \in \{0, 1, 2, 3, 4, 5, 6, 7, 8, 9\}$. A stacking pattern is found to be the global energy minima on the sliding plane, regardless of the *X*-site element, as shown in Figure 2a and Figure S2. The geometries of the ground-state bilayer penta-PdX_2 are depicted in Figure 2b and Figure S3. The ground-state bilayer penta-PdX_2 possesses C_{2v} symmetry with a 2-fold rotational axis c_{2b}, indicating spontaneous polarization along the [010] direction, as observed in experiment.[45] Next, we calculated the phonon spectra of the ground-state bilayer penta-PdX_2 to verify their dynamic stability, as no imaginary phonon modes are found throughout their first Brillouin zones (Figure 2c and Figure S3). To further investigate thermal stability, we performed *ab initio* molecular dynamics (AIMD) simulations at 300, 600, and 900 K, each with a duration of 10 ps and a time step of 1 fs. The total potential energies of the supercells fluctuated around constant values during the simulations at 900 K, and their geometries did not suffer significant distortion at the end of simulations, indicating that the ground-state bilayer penta-PdX_2 are thermally stable up to 900 K (Figure 2d and Figure S4). We examined the mechanical stability of the ground-state bilayer penta-PdX_2. The calculated elastic constants C_{ij}, listed in Table S1, satisfy the Born−Huang criteria,[52] namely, $C_{11} > 0$, $C_{22} > 0$, $C_{66} > 0$, and $C_{11}C_{22} > C_{12}^2$, indicating that they are mechanically stable. Based on such comprehensive stability examinations, the ground-state bilayer penta-PdX_2 is found to be stable dynamically, thermally, and mechanically. Therefore, the following discussions focus exclusively on the ground-state configuration.

Unlike out-of-plane polarization, the presence of in-plane polarization requires the structure to be semiconducting. Therefore, we calculated the band structures and the corresponding total and partial densities of states (DOS) of the bilayer penta-PdX_2 at the HSE06 level (Figure 3a and Figure S5). The bilayers penta-$PdTe_2$, penta-$PdSe_2$, and penta-PdS_2 are all semiconducting with indirect band gaps of 1.06, 1.52, and 1.61 eV, respectively. The DOS at the band edge is mainly contributed by the *d* orbitals of Pd atoms and *p* orbitals of *X* atoms, which is confirmed by the fatband analysis in Figure S6. The simultaneous presence of C_{2v} symmetry and semiconducting properties ensures the existence of spontaneous polarization in bilayer penta-PdX_2 along the [010] direction. To better understand the origin of spontaneous polarization in bilayer penta-PdX_2, we analyzed their deformation charge densities (Figure 3b and Figure S7), where the yellow and blue regions represent electron accumulation and depletion, respectively. After the centrosymmetric monolayers are stacked into bilayers, the centers of positive and negative charges separate along the [010] direction, forming electric dipole moments arranged in a well-ordered array, thereby establishing the observed spontaneous polarization.

Although previous experiments have confirmed that bilayer penta-$PdSe_2$ belongs to the C_{2v} polar point group,[45] the quantitative assessment of spontaneous polarization has remained unexplored. To obtain an accurate evaluation of

https://doi.org/10.1021/acs.jpclett.5c01522
J. Phys. Chem. Lett. 2025, 16, 7177−7186

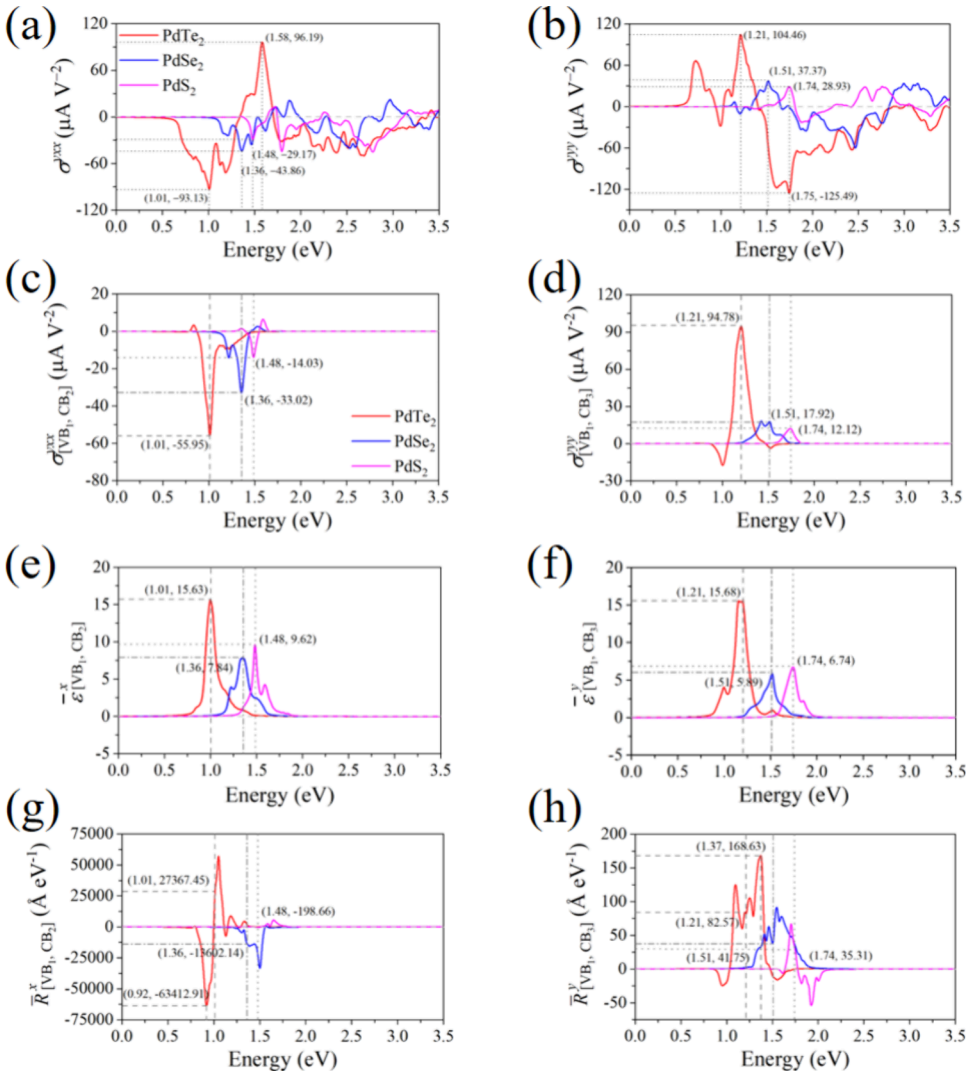

Figure 4. Shift current tensors (a) σ^{yxx} and (b) σ^{yyy} of the bilayer penta-PdX_2 (X = Te, Se, S). (c-h) The shift current, transition intensity, and aggregate shift vector contributed from the ($VB_1 \rightarrow CB_2$) and ($VB_1 \rightarrow CB_3$) pairs of the bilayer penta-PdX_2 (X = Te, Se, S).

the spontaneous polarization, a centrosymmetric nonpolar phase of bilayer penta-PdX_2 should be identified.[53] We found that the reference structure possesses C_{2h} nonpolar symmetry with *E* stacking configuration, as illustrated in Figure 3c. The value of spontaneous polarization is determined by adding or subtracting polarization quantum $P_q = N\ \boldsymbol{a}$ to obtain a continuously changing polarization curve, where *N* represents arbitrary integers, and $\boldsymbol{a}$ represents the length of a unit cell.[53] The calculated spontaneous polarizations P_s^y of bilayer penta-$PdTe_2$, penta-$PdSe_2$, and penta-PdS_2 are 1.70×10^{-10} C m^{-1}, 1.73×10^{-10} C m^{-1}, and 1.75×10^{-10} C m^{-1}, respectively, as shown in Figure S8, which aligns with the *yy* component of the Born effective charge tensor for the *X* atom $Z_{yy}^*(X)$, as shown in Figure 3d.

To explore the BPVE including shift and injection current, we first reproduced the DFT band structures by using the tight-binding Hamiltonian. As shown in Figure S9, they agree well with each other. For achieving well-converged BPVE results, an interpolated *k*-point mesh of $71 \times 71 \times 1$ was used following thorough testing, as illustrated in Figure S10. In the penta-PdX_2 system, the injection current is found to be significantly smaller than the shift current, as demonstrated in Figure S11 and Supplementary Note 1 in the Supporting Information, indicating that the shift current is the dominant contribution to the BPVE. We then examine the shift current, which arises from the displacement of the wave function center between the valence and conduction bands upon light excitation. Assuming a single laser source of linearly polarized light, the shift current conductivity is reduced to two independent in-plane nonvanishing shift current response tensors, $\sigma^{yxx}(\omega)$ and $\sigma^{yyy}(\omega)$. Since the magnitude of the shift current is larger than that of the injection current, the shift current is the major mechanism contributing to BPVE. It is worth noting that spin−orbit coupling (SOC) exerts only a minor influence on the shift current, as demonstrated in Figure S12. The bilayer penta-$PdTe_2$ demonstrates prominent shift current responses with primary peak values of 96.19 μA V^{-2} at 1.58 eV for $\sigma^{yxx}(\omega)$ and −125.49 μA V^{-2} at 1.75 eV for $\sigma^{yyy}(\omega)$, as shown in Figure 4a-b, which are comparable to those of theoretically proposed ternary pentagonal 2D structures[20,21] and significantly exceed the responses observed in many other polar systems.[11,54−56] The sign of the shift current tensor components reflects the relative orientation between the photocurrent and spontaneous polarization, with the positive (negative) values corresponding to the parallel (antiparallel) alignment resulting from the directional charge

https://doi.org/10.1021/acs.jpclett.5c01522
J. Phys. Chem. Lett. 2025, 16, 7177−7186

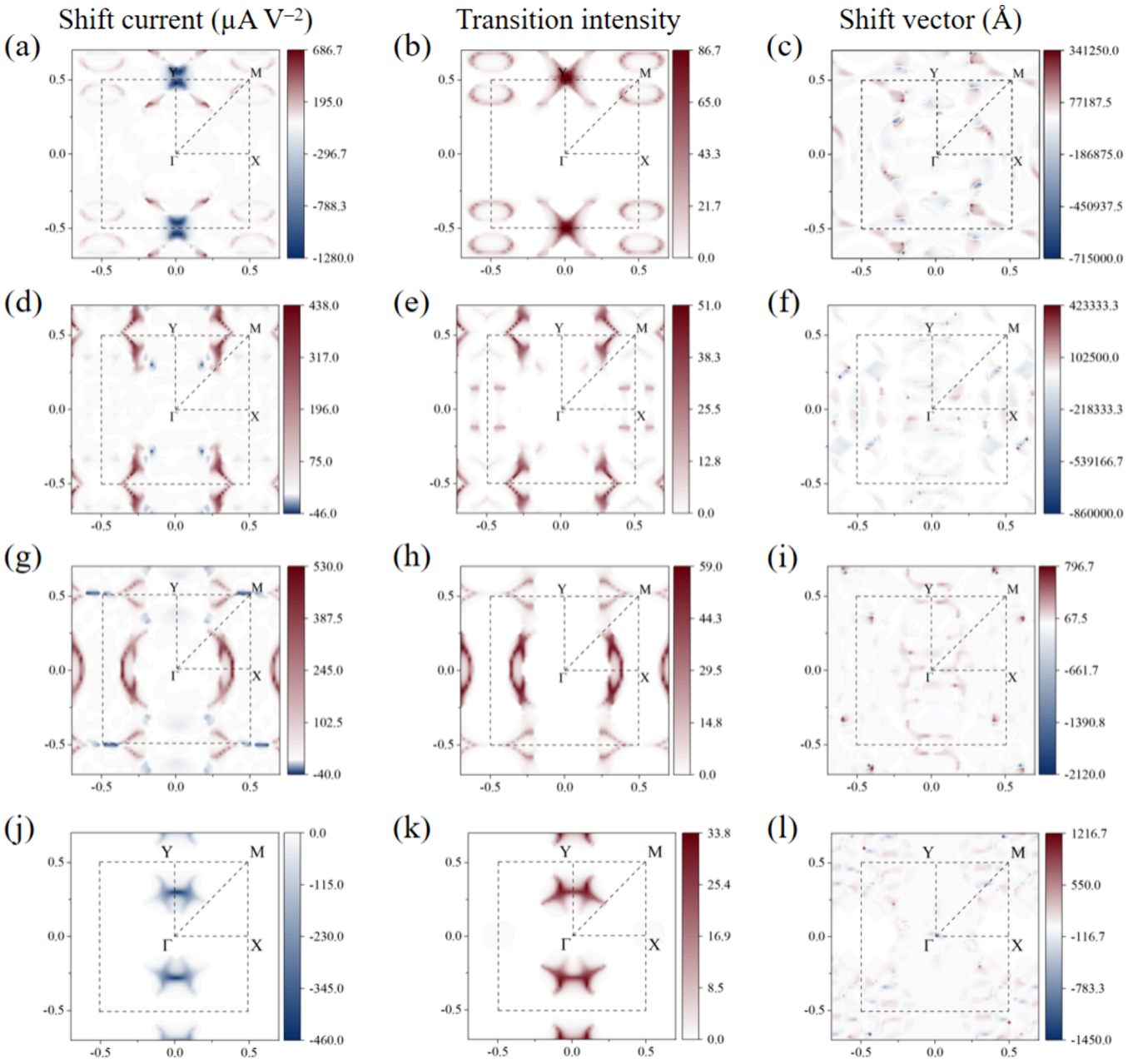

Figure 5. *k*-resolved shift current, transition intensity, and shift vector of bilayer penta-$PdTe_2$ between (a-c) VB_1 and CB_2 at $\hbar\omega$ = 1.01 eV, (d-f) VB_3 and CB_3 at $\hbar\omega$ = 1.58 eV, (g-i) VB_1 and CB_3 at $\hbar\omega$ = 1.21 eV, and (j-l) VB_4 and CB_1 at $\hbar\omega$ = 1.75 eV.

transfer during interband transitions.[57,58] On the other hand, the secondary peaks emerge at lower energies, namely, −93.13 μA V^{-2} at 1.01 eV for $\sigma^{yxx}(\omega)$ and 104.46 μA V^{-2} at 1.21 eV for $\sigma^{yyy}(\omega)$, while they are stronger than the peaks observed in bilayer penta-$PdSe_2$ and penta-PdS_2. Notice that strong BPVE responses are typically found in systems with stronger spontaneous polarization.[11,59] However, our results do not follow this trend, where the highest shift current is found in weakly polarized bilayer penta-$PdTe_2$, suggesting that the shift current and electric polarization may not be correlated in a specific way, especially in such complex materials.[6,10]

To gain deeper insights into the origin of the shift current responses, we systematically calculated the shift current tensors of 36 band pairs (VB_1−VB_6; CB_1−CB_6) at their respective peak positions, as detailed in Figure S13. We found that the main contributions to the characteristic peaks of 1.01 eV in $\sigma^{yxx}(\omega)$ and 1.21 eV in $\sigma^{yyy}(\omega)$ in bilayer penta-$PdTe_2$ are from the transition from the highest valence band (denoted VB_1) to the second lowest conduction band (denoted CB_2), and for the highest valence band (denoted VB_1) to the third lowest conduction band (denoted CB_3), respectively, which are denoted in Figure S14. This is because the profound transition matrix elements and joint density of states for these band pairs coincide in the Brillouin zone (Figures S15−S17). The shift current responses to photons between different band pairs are plotted in Figure S18. Apparently, bilayer penta-$PdTe_2$ exhibits a larger shift current response from VB_1 to CB_2 and VB_1 to CB_3 than those in bilayer penta-$PdSe_2$ and penta-PdS_2, as shown in Figure 4c-d.

To understand the microscopic mechanism for the strong BPVE in such pentagonal polar systems, we split the shift current tensor into two components, i.e., the shift vector R^b_{nm}

https://doi.org/10.1021/acs.jpclett.5c01522
J. Phys. Chem. Lett. 2025, 16, 7177−7186

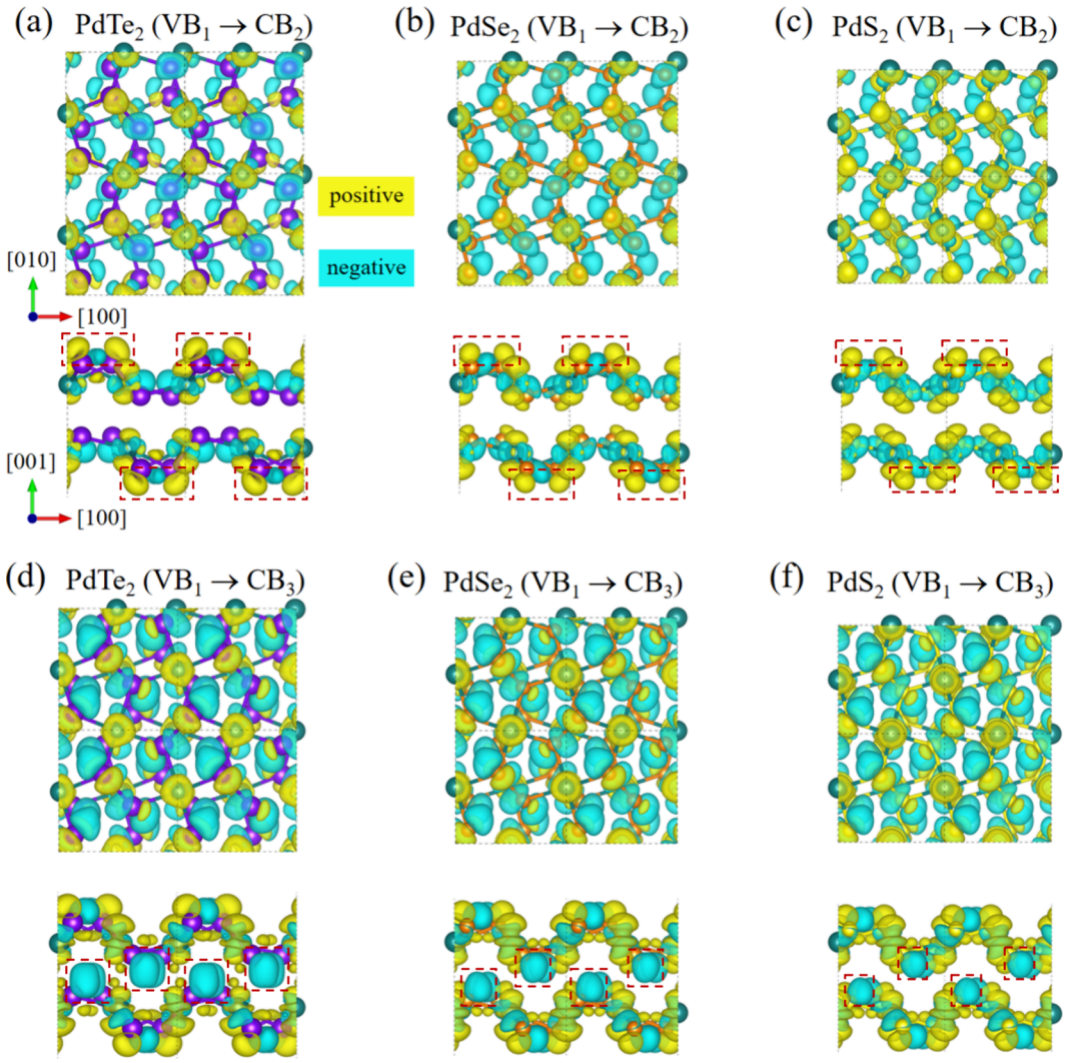

Figure 6. Charge density difference in bilayer penta-PdX_2 induced by electronic transition: (a-c) from VB_1 to CB_2 at the Y point of the Brillouin zone and (d-f) from VB_1 to CB_3 at the (0.375, 0, 0) point. Isosurface value is ± 0.002 Å^{-3}. Yellow and blue regions represent charge gain and loss, respectively. The scales of the three lattices are proportional to their lattice parameters. Red boxes highlight the representative regions for comparative analysis of charge density difference.

and transition intensity ε^b_{nm}. The shift vector characterizes the displacement of electrons in real space during the interband transition, while the transition intensity quantifies the optical adsorption, together determining the magnitude and direction of the shift current response.[11] The shift vector can be calculated with $R^b_{nm} = \mathrm{Im}[r^b_{mn} r^b_{nm;a} + r^b_{mn} r^b_{nm;a}] / |r^b_{nm}|^2$,[7] which describes the average displacement from band m to band n during the lifetime of an electron at reciprocal coordinate $\boldsymbol{k}$ after absorbing a photon. As an analytical tool, we integrated R^b_{nm} over the Brillouin zone between band m and band n:[21]

$$\overline{R^b}_{[n,m]}(\omega) = \int [\mathrm{d}\boldsymbol{k}] f_{nm} R^b_{nm} \delta(\omega_{nm} - \omega) \tag{3}$$

The separation of R^b_{nm} from the integral term in eq 1 leaves behind $f_{nm} |r^b_{nm}|^2$, whose integration is a measure of the transition intensity from band m to band n, written as[21]

$$\overline{\varepsilon}^b_{[n,m]}(\omega) = \frac{i\pi e^2}{\hbar} \int [\mathrm{d}\boldsymbol{k}] f_{nm} |r^b_{nm}|^2 \delta(\omega_{nm} - \omega) \tag{4}$$

The peak position of $\overline{\varepsilon}^x_{[\mathrm{VB}_1,\mathrm{CB}_2]}(\omega)$ is consistent with that of $\sigma^{yxx}_{[\mathrm{VB}_1,\mathrm{CB}_2]}(\omega)$, and the peak position of $\overline{\varepsilon}^y_{[\mathrm{VB}_1,\mathrm{CB}_3]}(\omega)$ is consistent with that of $\sigma^{yyy}_{[\mathrm{VB}_1,\mathrm{CB}_3]}(\omega)$, as shown in Figure 4e-f. Although the transition intensity of bilayer $PdSe_2$ is smaller than that in bilayer penta-PdS_2, the shift current $[\sigma^{yxx}_{[\mathrm{VB}_1,\mathrm{CB}_2]}(\omega)$ and $\sigma^{yyy}_{[\mathrm{VB}_1,\mathrm{CB}_3]}(\omega)]$ in bilayer penta-$PdSe_2$ is larger than that in bilayer penta-PdS_2. This is because the shift vector $[\overline{R}^x_{[\mathrm{VB}_1,\mathrm{CB}_2]}(\omega)$ and $\overline{R}^y_{[\mathrm{VB}_1,\mathrm{CB}_3]}(\omega)]$ dominates the magnitude of the shift current response, as shown in Figure 4g-h. In bilayer penta-$PdTe_2$, both the transition intensity and shift vector are larger compared to those of bilayer penta-$PdSe_2$ and bilayer penta-PdS_2, resulting in its larger shift current response. Interestingly, in such pentagonal bilayer polar materials, the shift vector exhibits strong anisotropy, as shown in Figure 4g,h. In bilayer penta-$PdTe_2$, $\overline{R}^y_{[\mathrm{VB}_1,\mathrm{CB}_3]}(\omega)$ has a peak value of 168.63 Å eV^{-1} at 1.37 eV, while $\overline{R}^x_{[\mathrm{VB}_1,\mathrm{CB}_2]}(\omega)$ possesses an enormous peak value of − 63412.91 Å eV^{-1} at 1.37 eV, which is more than 2 orders of magnitude larger than that in $\overline{R}^y_{[\mathrm{VB}_1,\mathrm{CB}_3]}(\omega)$.

https://doi.org/10.1021/acs.jpclett.5c01522
J. Phys. Chem. Lett. 2025, 16, 7177−7186

To understand the previous aggregate quantities, we further plotted the *k*-resolved values. The *k*-resolved shift current, transition intensity, and shift vector of the bilayer penta-$PdTe_2$ at respective major peak positions of 1.01, 1.21, 1.58, and 1.75 eV are shown in Figure 5. The shift current contains most features of the transition intensity in the bilayer penta-$PdTe_2$. The primary contribution to the shift current in bilayer penta-$PdTe_2$ at the peak position of 1.01 eV comes from the transition at the high-symmetry point Y. Meanwhile, the contributions at the peak positions of 1.21, 1.58, and 1.75 eV originate from transitions within the interior of the Brillouin zone as well as along the high-symmetry paths. Regarding the shift vector, the values of $R^{x}_{[VB_1,CB_2]}(1.01eV)$ and $R^{x}_{[VB_3,CB_3]}(1.58eV)$ in bilayer penta-$PdTe_2$ are significantly larger than those of $R^{y}_{[VB_1,CB_3]}(1.21eV)$ and $R^{y}_{[VB_4,CB_1]}(1.75eV)$, consistent with the previously calculated aggregate shift vectors. Moreover, because the transition intensity is always positive ($\propto |r^{b}_{nm}|^2$), the sign of the shift current is consistent with that of the shift vector. Unlike the transition intensity, the distribution of the shift vector is discontinuous throughout the Brillouin zone. Both strong positive and negative values of the shift vector are observed in bilayer penta-$PdTe_2$, leading to a cancellation effect that reduces the net current after integration over the Brillouin zone. To compare the results of bilayer penta-$PdTe_2$ with those of bilayer penta-$PdSe_2$ and bilayer penta-PdS_2, we plotted the *k*-resolved values at their characteristic energy position on a unified color bar, as shown in Figures S19−S20. The transition intensities of bilayer penta-$PdTe_2$, penta-$PdSe_2$, and penta-PdS_2 exhibit entirely different distributions. The distributions of both transition intensity and shift vector in bilayer penta-$PdTe_2$ are more extensive compared to those in bilayer penta-$PdSe_2$ and bilayer penta-PdS_2, consequently leading to the enhanced shift current response in bilayer penta-$PdTe_2$.

To investigate the origin of the high shift current response in bilayer penta-$PdTe_2$ compared to bilayer penta-$PdSe_2$ and penta-PdS_2, which is counterintuitive given the lowest spontaneous polarization of bilayer penta-$PdTe_2$ among the investigated systems, we analyzed their related electronic properties. Among the penta-PdX_2 systems, bilayer penta-$PdTe_2$ exhibits the lowest light absorption onset due to its smallest band gap, and thus the strongest adsorption occurs at low energy, i.e., <1.5 eV (see Figure S21). Besides, the transition dipole moment analysis from VB_1 to CB_2 and from VB_1 to CB_3 of bilayer penta-PdX_2 (see Figure S22) demonstrates superior dipole coupling strength in bilayer penta-$PdTe_2$, thus leading to its larger shift current response from VB_1 to CB_2 and VB_1 to CB_3 than those in bilayer penta-$PdSe_2$ and penta-PdS_2. We then calculate the band-decomposed charge density for bilayer penta-PdX_2 at two critical k-points: (i) VB_1 and CB_2 at the Y point and (ii) VB_1 and CB_3 at the (0.375, 0, 0) point in the Brillouin zone (Figures S23−S24), where the k-point-resolved shift current reached its peak in bilayer penta-$PdTe_2$. The difference in charge density, shown in Figure 6, illustrates the charge transfer responsible for the peak shift current. In bilayer penta-PdX_2, the charge redistribution following photoexcitation shows distinct spatial characteristics; for $VB_1 \rightarrow CB_2$ at Y-point, Te dimers exhibit significantly larger out-of-plane lone-pair electron lobes (yellow regions in Figure 6a-c) compared to Se/S dimers. Similarly, for $VB_1 \rightarrow CB_3$ at the (0.375, 0, 0) point, Te dimers show a more pronounced interlayer charge delocalization (blue regions in Figure 6d-f). The enhanced displacement of electron density in Te dimers stems from weaker p_z-orbital binding compared with Se/S dimers, resulting from reduced attraction between valence electrons and the heavy Te ion cores. The enhanced charge redistribution in Te dimers is the main reason for the stronger shift current response in bilayer penta-$PdTe_2$ as compared to the bilayer penta-$PdSe_2$ and penta-PdS_2 counterparts.

In summary, we systematically explored the evolution of electric polarization across the entire stacking configuration space of bilayer penta-$PdTe_2$ through symmetry analysis. First-principles calculations reveal that the ground state of bilayer penta-$PdTe_2$ exhibits a significant spontaneous polarization, $P^{y}_{s} = 1.70 \times 10^{-10}$ C m^{-1}, resulting in exceptionally large shift currents reaching up to 125.49 μA V^{-2}, which is substantially higher than those observed in bilayer penta-$PdSe_2$ (43.86 μA V^{-2}) and penta-PdS_2 (29.17 μA V^{-2}). The enhanced shift current response in bilayer penta-$PdTe_2$ is attributed to its stronger transition intensity and shift vector compared to those of its $PdSe_2$ and PdS_2 counterparts. These findings highlight the tuning of stacking configurations in pentagonal layered materials as an effective strategy for designing BPVE materials, providing new opportunities for the potential applications of experimentally synthesized pentagonal compounds in photovoltaics.

■ ASSOCIATED CONTENT

Supporting Information

The Supporting Information is available free of charge at https://pubs.acs.org/doi/10.1021/acs.jpclett.5c01522.

Additional data and figures, including the geometries of monolayer penta-PdX_2 (X = Te, Se, S), the convergence test of the calculated shift current, shift current, injection current, band structure fitting by using the Wannier functions, potential energy surface, polarization, thermal and mechanical stability, phonon spectra, deformation charge density, and optical absorption (PDF)

■ AUTHOR INFORMATION

Corresponding Authors

Yiheng Shen − *Materials Genome Institute, Shanghai University, Shanghai 200444, China*; Email: yihengshen@shu.edu.cn

Yaguang Guo − *Department of Physics, School of Physical Science and Engineering, Beijing Jiaotong University, Beijing 100044, China*; orcid.org/0000-0001-5659-3528; Email: ygguo@bjtu.edu.cn

Qian Wang − *School of Materials Science and Engineering, Peking University, Beijing 100871, China*; orcid.org/0000-0002-9766-4617; Email: qianwang2@pku.edu.cn

Authors

Changsheng Hou − *School of Materials Science and Engineering, Peking University, Beijing 100871, China*

Jiaqi Xin − *Department of Physics, School of Physical Science and Engineering, Beijing Jiaotong University, Beijing 100044, China*

Complete contact information is available at: https://pubs.acs.org/10.1021/acs.jpclett.5c01522

https://doi.org/10.1021/acs.jpclett.5c01522
J. Phys. Chem. Lett. 2025, 16, 7177−7186

Notes

The authors declare no competing financial interest.

■ ACKNOWLEDGMENTS

This work is partially supported by grants from the National Natural Science Foundation of China (Grant No. NSFC-12274007), and is also supported by the High-Performance Computing Platform of Peking University, China.

■ REFERENCES

(1) Auston, D. H.; Glass, A. M.; Ballman, A. A. Optical rectification by impurities in polar crystals. *Phys. Rev. Lett.* **1972**, *28*, 897−900.
(2) Glass, A. M.; von der Linde, D.; Negran, T. J. High-voltage bulk photovoltaic effect and the photorefractive process in $LiNbO_3$. *Appl. Phys. Lett.* **1974**, *25*, 233−235.
(3) Von Baltz, R.; Kraut, W. Theory of the bulk photovoltaic effect in pure crystals. *Phys. Rev. B* **1981**, *23*, 5590−5596.
(4) Yang, M. M.; Kim, D. J.; Alexe, M. Flexo-photovoltaic effect. *Science* **2018**, *360*, 904−907.
(5) Yang, S. Y.; Seidel, J.; Byrnes, S. J.; Shafer, P.; Yang, C. H.; Rossell, M. D.; Yu, P.; Chu, Y. H.; Scott, J. F.; Ager, J. W.; Martin, L. W.; Ramesh, R. Above-bandgap voltages from ferroelectric photovoltaic devices. *Nat. Nanotechnol.* **2010**, *5*, 143−147.
(6) Young, S. M.; Rappe, A. M. First principles calculation of the shift current photovoltaic effect in ferroelectrics. *Phys. Rev. Lett.* **2012**, *109*, 116601.
(7) Sipe, J. E.; Shkrebtii, A. I. Second-order optical response in semiconductors. *Phys. Rev. B* **2000**, *61*, 5337−5352.
(8) Sturman, B. I. Ballistic and shift currents in the bulk photovoltaic effect theory. *Phys. Usp.* **2020**, *63*, 407.
(9) Belinicher, V. I.; Sturman, B. I. The relation between shift and ballistic currents in the theory of photogalvanic effect. *Ferroelectrics* **1988**, *83*, 29−34.
(10) Tan, L. Z.; Zheng, F.; Young, S. M.; Wang, F.; Liu, S.; Rappe, A. M. Shift current bulk photovoltaic effect in polar materials—hybrid and oxide perovskites and beyond. *npj Comput. Mater.* **2016**, *2*, 16026.
(11) Rangel, T.; Fregoso, B. M.; Mendoza, B. S.; Morimoto, T.; Moore, J. E.; Neaton, J. B. Large bulk photovoltaic effect and spontaneous polarization of single-layer monochalcogenides. *Phys. Rev. Lett.* **2017**, *119*, 067402.
(12) Li, L.; Liu, X.; Li, Y.; Xu, Z.; Wu, Z.; Han, S.; Tao, K.; Hong, M.; Luo, J.; Sun, Z. Two-dimensional hybrid perovskite-type ferroelectric for highly polarization-sensitive shortwave photodetection. *J. Am. Chem. Soc.* **2019**, *141*, 2623−2629.
(13) Tiwari, R. P.; Birajdar, B.; Ghosh, R. K. First-principles calculation of shift current bulk photovoltaic effect in two-dimensional α-In_2Se_3. *Phys. Rev. B* **2020**, *101*, 235448.
(14) Li, Y.; Fu, J.; Mao, X.; Chen, C.; Liu, H.; Gong, M.; Zeng, H. Enhanced bulk photovoltaic effect in two-dimensional ferroelectric $CuInP_2S_6$. *Nat. Commun.* **2021**, *12*, 5896.
(15) Li, L.; Wu, M. Binary compound bilayer and multilayer with vertical polarizations: two-dimensional ferroelectrics, multiferroics, and nanogenerators. *ACS Nano* **2017**, *11*, 6382−6388.
(16) Ji, J.; Yu, G.; Xu, C.; Xiang, H. J. General theory for bilayer stacking ferroelectricity. *Phys. Rev. Lett.* **2023**, *130*, 146801.
(17) Zhang, S.; Zhou, J.; Wang, Q.; Chen, X.; Kawazoe, Y.; Jena, P. Penta-graphene: a new carbon allotrope. *Proc. Natl. Acad. Sci. U.S.A.* **2015**, *112*, 2372−2377.
(18) Atinafu, D. G.; Dong, W.; Hou, C.; Andriamitantsoa, R. S.; Wang, J.; Huang, X.; Gao, H.; Wang, G. A facile one-step synthesis of porous N-doped carbon from MOF for efficient thermal energy storage capacity of shape-stabilized phase change materials. *Mater. Today Energy* **2019**, *12*, 239−249.
(19) Shen, Y.; Wang, Q. Pentagon-based 2D materials: classification, properties and applications. *Phys. Rep.* **2022**, *964*, 1−42.
(20) Guo, Y.; Zhou, J.; Xie, H.; Chen, Y.; Wang, Q. Screening transition metal-based polar pentagonal monolayers with large piezoelectricity and shift current. *npj Comput. Mater.* **2022**, *8*, 40.
(21) Xin, J.; Guo, Y.; Wang, Q. Screening two-dimensional pyroelectric materials based on pentagonal chains with large shift current. *Phys. Rev. Mater.* **2023**, *7*, 074001.
(22) Guo, Y.; Zhang, C.; Zhou, J.; Wang, Q.; Jena, P. Lattice dynamic and instability in pentasilicene: a light single-element ferroelectric material with high curie temperature. *Phys. Rev. Appl.* **2019**, *11*, 064063.
(23) Gudelli, V. K.; Guo, G. Y. Large bulk photovoltaic effect and second-harmonic generation in few-layer pentagonal semiconductors PdS_2 and $PdSe_2$. *New J. Phys.* **2021**, *23*, 093028.
(24) Hou, C.; Shen, Y.; Wang, Q.; Yoshikawa, A.; Kawazoe, Y.; Jena, P. In-plane sliding ferroelectricity realized in penta-$PdSe_2$/penta-$PtSe_2$ van der waals heterostructure. *ACS Nano* **2024**, *18*, 16923−16933.
(25) Hou, C.; Shen, Y.; Wang, Q. Metallic sliding ferroelectricity in trilayer penta-NiN_2. *Adv. Funct. Mater.* **2025**, *35*, 2421311.
(26) Liu, L.; Ji, Y.; Bianchi, M.; Hus, S. M.; Li, Z.; Balog, R.; Miwa, J. A.; Hofmann, P.; Li, A. P.; Zemlyanov, D. Y.; Li, Y.; Chen, Y. P. A metastable pentagonal 2D material synthesized by symmetry-driven epitaxy. *Nat. Mater.* **2024**, *23*, 1339−1346.
(27) Kresse, G.; Furthmüller, J. Efficient iterative schemes for ab initio total-energy calculations using a plane-wave basis set. *Phys. Rev. B* **1996**, *54*, 11169−11186.
(28) Teter, M. P.; Payne, M. C.; Allan, D. C. Solution of Schrodinger's equation for large systems. *Phys. Rev. B* **1989**, *40*, 12255−12263.
(29) Blöchl, P. E. Projector augmented-wave method. *Phys. Rev. B* **1994**, *50*, 17953−17979.
(30) Bučko, T.; Hafner, J.; Lebègue, S.; Ángyán, J. G. Improved description of the structure of molecular and layered crystals: ab initio DFT calculations with van der waals corrections. *J. Phys. Chem. A* **2010**, *114*, 11814−11824.
(31) Monkhorst, H. J.; Pack, J. D. Special points for brillouin-zone integrations. *Phys. Rev. B* **1976**, *13*, 5188−5192.
(32) Heyd, J.; Scuseria, G. E.; Ernzerhof, M. Hybrid functionals based on a screened coulomb potential. *J. Chem. Phys.* **2003**, *118*, 8207−8215.
(33) Parlinski, K.; Li, Z. Q.; Kawazoe, Y. First-principles determination of the soft mode in Cubic ZrO_2. *Phys. Rev. Lett.* **1997**, *78*, 4063−4066.
(34) Togo, A.; Tanaka, I. First principles phonon calculations in materials science. *Scr. Mater.* **2015**, *108*, 1−5.
(35) Nosé, S. A unified formulation of the constant temperature molecular dynamics methods. *J. Chem. Phys.* **1984**, *81*, 511−519.
(36) King-Smith, R. D.; Vanderbilt, D. Theory of polarization of crystalline solids. *Phys. Rev. B* **1993**, *47*, 1651−1654.
(37) Mills, G.; Jónsson, H. Quantum and thermal effects in H_2 dissociative adsorption: evaluation of free energy barriers in multidimensional quantum systems. *Phys. Rev. Lett.* **1994**, *72*, 1124−1127.
(38) Henkelman, G.; Arnaldsson, A.; Jónsson, H. A fast and robust algorithm for bader decomposition of charge density. *Comput. Mater. Sci.* **2006**, *36*, 354−360.
(39) Tang, W.; Sanville, E.; Henkelman, G. A grid-based bader analysis algorithm without lattice bias. *J. Condens. Matter Phys.* **2009**, *21*, 084204.
(40) Sipe, J. E.; Ghahramani, E. Nonlinear optical response of semiconductors in the independent-particle approximation. *Phys. Rev. B* **1993**, *48*, 11705−11722.
(41) Ibañez-Azpiroz, J.; Tsirkin, S. S.; Souza, I. Ab initio calculation of the shift photocurrent by Wannier interpolation. *Phys. Rev. B* **2018**, *97*, 245143.
(42) Mostofi, A. A.; Yates, J. R.; Lee, Y. S.; Souza, I.; Vanderbilt, D.; Marzari, N. Wannier90: a tool for obtaining maximally-localised wannier functions. *Comput. Phys. Commun.* **2008**, *178*, 685−699.
(43) Mostofi, A. A.; Yates, J. R.; Pizzi, G.; Lee, Y. S.; Souza, I.; Vanderbilt, D.; Marzari, N. An updated version of wannier90: A tool for obtaining maximally-localised wannier functions. *Comput. Phys. Commun.* **2014**, *185*, 2309−2310.

https://doi.org/10.1021/acs.jpclett.5c01522
J. Phys. Chem. Lett. 2025, 16, 7177−7186

(44) Shi, Y.; Zhou, J. Coherence control of directional nonlinear photocurrent in spatially symmetric systems. *Phys. Rev. B* **2021**, *104*, 155146.
(45) Oyedele, A. D.; Yang, S.; Liang, L.; Puretzky, A. A.; Wang, K.; Zhang, J.; Yu, P.; Pudasaini, P. R.; Ghosh, A. W.; Liu, Z.; Rouleau, C. M.; Sumpter, B. G.; Chisholm, M. F.; Zhou, W.; Rack, P. D.; Geohegan, D. B.; Xiao, K. $PdSe_2$: pentagonal two-dimensional layers with high air stability for electronics. *J. Am. Chem. Soc.* **2017**, *139*, 14090−14097.
(46) Zhang, X.; Su, G.; Lu, J.; Yang, W.; Zhuang, W.; Han, K.; Wang, X.; Wan, Y.; Yu, X.; Yang, P. Centimeter-scale few-layer PdS_2: fabrication and physical properties. *ACS Appl. Mater.* **2021**, *13*, 43063−43074.
(47) Neumann, F. E.; Meyer, O. E. *Vorlesungen über die Theorie der Elastizität der festen Körper und des Lichtäthers*; B. G. Teubner-Verlag: Leipzig, 1885.
(48) Wang, K.; Xu, R.; Gao, F.; Xu, S.; Hao, S.; Fan, C.; Zhang, Y.; Wei, Y.; Xue, X.; Hao, G. Controlled epitaxial growth of strain-induced large-area bilayer MoS_2 by chemical vapor deposition based on two-stage strategy. *Mater. Today Phys.* **2024**, *46*, 101501.
(49) Qin, G. Q.; Jing, F. M.; Hao, T. Y.; Jiang, S. L.; Zhang, Z. Z.; Cao, G.; Song, X. X.; Guo, G. P. Switching spin filling sequence in a bilayer graphene quantum dot through trigonal warping. *Phys. Rev. Lett.* **2025**, *134*, 036301.
(50) Yasuda, K.; Wang, X.; Watanabe, K.; Taniguchi, T.; Jarillo-Herrero, P. Stacking-engineered ferroelectricity in bilayer boron nitride. *Science* **2021**, *372*, 1458−1462.
(51) Lan, Y. S.; Chen, X. R.; Hu, C. E.; Cheng, Y.; Chen, Q. F. Penta-PdX_2 (X = S, Se, Te) monolayers: promising anisotropic thermoelectric materials. *J. Mater. Chem. A* **2019**, *7*, 11134−11142.
(52) Born, M.; Huang, K.; Lax, M. Dynamical theory of crystal lattices. *Am. J. Phys.* **1955**, *23*, 474.
(53) Spaldin, N. A. A beginner's guide to the modern theory of polarization. *J. Solid State Chem.* **2012**, *195*, 2−10.
(54) Qiu, Y.; Sun, Y.; Shen, H. X.; Fu, H. X.; Duan, M. Y.; Cheng, C. The shift current photovoltaic effect response in wurtzite and zinc blende semiconductors via first-principles calculations. *Phys. Chem. Chem. Phys.* **2024**, *26*, 27152−27162.
(55) Zhang, Y.; de Juan, F.; Grushin, A. G.; Felser, C.; Sun, Y. Strong bulk photovoltaic effect in chiral crystals in the visible spectrum. *Phys. Rev. B* **2019**, *100*, 245206.
(56) Ai, H.; Kong, Y.; Liu, D.; Li, F.; Geng, J.; Wang, S.; Lo, K. H.; Pan, H. 1T‴ transition-metal dichalcogenides: strong bulk photovoltaic effect for enhanced solar-power harvesting. *J. Phys. Chem. C* **2020**, *124*, 11221−11228.
(57) Strasser, A.; Wang, H.; Qian, X. Nonlinear optical and photocurrent responses in janus MoSSe monolayer and MoS_2−MoSSe van der Waals heterostructure. *Nano Lett.* **2022**, *22*, 4145−4152.
(58) Yang, L.; Li, L.; Yu, Z. M.; Wu, M.; Yao, Y. Two-dimensional topological ferroelectric metal with giant shift current. *Phys. Rev. Lett.* **2024**, *133*, 186801.
(59) Xu, F.; Su, H.; Gong, Z.; Wei, Y.; Jin, H.; Guo, H. Controllable ferroelectricity and bulk photovoltaic effect in elemental group-V monolayers through strain engineering. *Phys. Rev. B* **2022**, *106*, 195418.

https://doi.org/10.1021/acs.jpclett.5c01522
J. Phys. Chem. Lett. 2025, 16, 7177−7186